Advanced Functional Materials

ADVANCED FUNCTIONAL MATERIALS
www.afm-journal.de

RESEARCH ARTICLE

Synergistic Piezoelectricity and Lubrication in an Injectable Hydrogel for Osteochondral Regeneration

Dengjie Yu[1,2,3,4] | Longfei Li[3,5,6] | Xi Cui[2] | Binbin Yang[1] | Boyang Pei[7] | Jiaxuan Li[3,6] | Ruizeng Luo[2] | Yadong Zhang[1,7] | Yusheng Li[8] | Zhou Li[2,5] | Yantao Zhao[1,9]

[1]Department of Orthopedics, the Fourth Medical Center of PLA General Hospital, Beijing, P. R. China | [2]Vita Tech Innovation Center, School of Clinical Medicine, Tsinghua Changgung Hospital, Tsinghua University, Beijing, P. R. China | [3]Beijing Institute of Nanoenergy and Nanosystems, Chinese Academy of Sciences, Beijing, P. R. China | [4]Medical School of Chinese PLA, Beijing, P. R. China | [5]School of Biomedical Engineering, Tsinghua University, Beijing, P. R. China | [6]School of Nanoscience and Engineering, University of Chinese Academy of Sciences, Beijing, P. R. China | [7]Department of Orthopedics, the Fifth Medical Center of PLA General Hospital, Beijing, P. R. China | [8]Department of Orthopedics, Xiangya Hospital, Central South University, Changsha, P. R. China | [9]Beijing Engineering Research Center of Orthopedics Implants, Beijing, P. R. China

Correspondence: Yadong Zhang (drzyd@126.com) | Yusheng Li (liyusheng@csu.edu.cn) | Zhou Li (li_zhou@tsinghua.edu.cn) | Yantao Zhao (biodoctor1981@163.com)

Received: 10 January 2026 | **Revised:** 4 April 2026 | **Accepted:** 15 April 2026

Keywords: lubrication | osteochondral regeneration | piezoelectric stimulation | tissue engineering

ABSTRACT

The repair of osteochondral defects remains a challenge due to the limited self-repair capability of cartilage tissue. We present an injectable, biodegradable hydrogel scaffold integrating piezoelectricity with surface lubrication to mimic the native joint microenvironment. The scaffold comprises a methacrylated gelatin (GelMA) matrix reinforced with piezoelectric poly(L-lactic acid) (PLLA) fibers, fabricated via in situ photocuring. A poly (2-methacryloyloxyethyl phosphorylcholine) (PMPC) lubricating layer is subsequently grafted using residual photoinitiators, creating a stable dual-functional system (G-P-M). Mechanistically, the PMPC coating dissipates harmful shear stress, while the internal piezoelectric network converts physiological mechanical loads into electrical signals. This synergistic biophysical modulation significantly enhances the osteogenic and chondrogenic differentiation of bone marrow mesenchymal stem cells (BMSCs) and attenuates chondrocyte senescence in vitro. In a rat full-thickness osteochondral defect model, the G-P-M scaffold demonstrated superior regeneration efficacy driven by the combined effects of lubrication and piezoelectric stimulation. This study offers a bioinspired strategy integrating stress dissipation and electrophysiological cues for osteochondral tissue engineering.

1 | Introduction

Articular cartilage is a critical load-bearing tissue prone to damage from overuse, injury, and abnormal loading [1]. Due to its avascular, aneural nature and low cellularity, the intrinsic regenerative capacity of cartilage is limited [2, 3]. While clinical interventions like microfracture and autologous chondrocyte implantation offer temporary relief, these conventional treatments often fail to restore hyaline cartilage, resulting in fibrocartilage formation and eventual tissue degeneration [4, 5]. Moreover, while tissue engineering strategies relying on biochemical factors or stem cells have shown promise, such approaches are hindered by the rapid depletion of exogenous regenerative signals and the inability to adequately recapitulate the native biophysical microenvironment governing cartilage homeostasis [6, 7]. Consequently, reinstating the native biophysical microenvironment

Dengjie Yu, Longfei Li, and Xi Cui contributed equally to the work.

specifically by mimicking endogenous signaling has emerged as a pivotal alternative paradigm to overcome these therapeutic limitations [8].

Notably, natural bone and cartilage are intrinsically piezoelectric, converting physiological loads into endogenous electrical signals that regulate cell fate and tissue maintenance [9, 10]. Piezoelectric materials, activated by movement or ultrasound, can mimic this bioelectricity to potentate osteochondral regeneration [11–13]. However, the harsh mechanical environment within the knee joint poses a significant challenge to the clinical translation of piezoelectric scaffolds. The knee joint, particularly load-bearing regions like the femoral condyle, endures extreme compressive stresses [14]. In healthy, the cartilage surface acts as a near-frictionless interface. Conversely, injury disrupts this lubrication, drastically increasing the coefficient of friction and interfacial shear stress [15]. This presents a fundamental dilemma for piezoelectric applications: while physiological compression is essential to activate piezoelectricity, the excessive shear forces inherent to injured joints not only compromise the structural integrity of the scaffold but also severely undermine the therapeutic efficacy of the piezoelectric stimulation [16, 17]. Consequently, effective surface lubrication is indispensable to preserve piezoelectric efficacy, necessitating a synergistic strategy that decouples these forces by dissipating harmful shear while harvesting beneficial compression [18].

Herein, we developed an injectable, biodegradable hydrogel system that synergistically integrates piezoelectricity and surface lubrication to reconstruct the osteochondral microenvironment. We fabricated a scaffold comprising a gelatin methacryloyl (GelMA) matrix reinforced with piezoelectric poly(L-lactic acid) (PLLA) fibers through a streamlined in situ photocuring process. Crucially, utilizing a shared photoinitiator strategy, a biomimetic poly (2-methacryloyloxyethyl phosphorylcholine) (PMPC) lubricating layer is grafted onto the scaffold surface during the same UV curing window. (Figure 1a) [19]. This design establishes a functional mechanical interface: following minimally invasive injection (Figure 1b), the PMPC coating acts as a sacrificial barrier to dissipate excessive shear stress, thereby shielding the nascent tissue. Concurrently, the internal network transmits physiological compressive loads to the PLLA fibers, activating in situ piezoelectric stimulation. (Figure 1c) [20]. This dual-action mechanism enhances osteochondral regeneration and attenuates chondrocyte senescence by restoring a favorable electromechanical niche, offering a robust bioinspired strategy for effective osteochondral defect repair.

2 | Results and Discussions

2.1 | Fabrication and Characterization of the Piezoelectric Hydrogel

For osteochondral defect repair, a scaffold with good biocompatibility and mechanical support is essential [21]. GelMA hydrogel was selected as the base material due to its inherent biocompatibility and tunable mechanical properties [22]. To introduce photocrosslinkable sites, gelatin was chemically modified via methacrylation to synthesize GelMA. The successful synthesis of GelMA was confirmed by ^{1}H NMR spectroscopy (Figure 2a), which revealed two characteristic new peaks at 5.32 ppm and 5.56 ppm [23]. The GelMA hydrogel prepared at 10 wt.% can be molded after 1 min of 365 nm UV exposure (Figure S1). Characterization of the resultant hydrogel further confirmed its favorable porous morphology and uniform elemental distribution (Figure 2b).

To impart piezoelectric properties, PLLA was incorporated into the GelMA. PLLA is a well-established biodegradable and biocompatible polymer known for its intrinsic piezoelectricity [24, 25]. Specifically, the oriented PLLA nanofibers (Figure S2) were prepared via electrospinning. These nanofiber membranes were then cryogenically sectioned into uniform short fibers approximately 30 μm in length (Figure 2c) to facilitate their homogeneous dispersion within the hydrogel matrix. When PLLA short fibers were incorporated into the GelMA hydrogel at a concentration of 5 mg/mL, Figure 2d and Figure S3 reveal their morphology, with PLLA short fibers uniformly distributed within the pores of the GelMA matrix. Moreover, the GelMA-PLLA hydrogel exhibits excellent injectability, enabling smooth writing of the “NBL” logo, and complete crosslinking within 1 min of UV exposure (Figure 2e).

2.2 | Integrating Lubrication Properties Onto the Piezoelectric Hydrogel

Given the critical importance of lubrication properties for articular cartilage repair, we developed a strategy for fabricating PMPC lubrication coatings onto the hydrogel surface. PMPC is well-recognized for its outstanding biocompatibility and excellent lubrication performance, primarily attributed to its zwitterionic nature and ability to form a highly hydrated layer, making it widely applied in cartilage repair and surface functionalization [26, 27]. Upon immersing the partially photocrosslinked GelMA hydrogel in an MPC monomer solution, the residual I2959 effectively triggered the free radical polymerization of MPC preferentially on the hydrogel surface (Figure 2f). Figure 2g displays the surface morphology and elemental distribution of the hydrogel, revealing uniform phosphorus distribution. In stark contrast, the interior of the hydrogel contains virtually no phosphorus (Figure S4). The elemental distribution on the surface and cross-section of G-PMPC further indicates that PMPC is primarily located on the top surface of the hydrogel (Figure S5). This occurs because during immersion in the MPC solution, the partially formed hydrogel structure impedes the deep polymerization of MPC, thus leaving most of it polymerizing on the surface. Figure 2h and Figure S6 further demonstrate the effective modification of PMPC, as evidenced by the presence of the phosphorus element exclusively in the modified GelMA-PMPC hydrogel (G-PMPC) compared to the unmodified GelMA hydrogel (G).

More importantly, the successful grafting of PMPC endows the hydrogel scaffold with excellent lubricating properties (Figure 2i). As shown in Figure 2j, the coefficient of friction (COF) decreased from 0.0842 in the GelMA hydrogel itself to 0.0083. The COF of the G-PMPC hydrogel remained stable at 0.0089 after 18 000 s of wear (Figure S7), and the characteristic element (P) was still uniformly present in the hydrogel’s wear zone, indicating the long-term stability of the PMPC surface coating (Figure S8). This

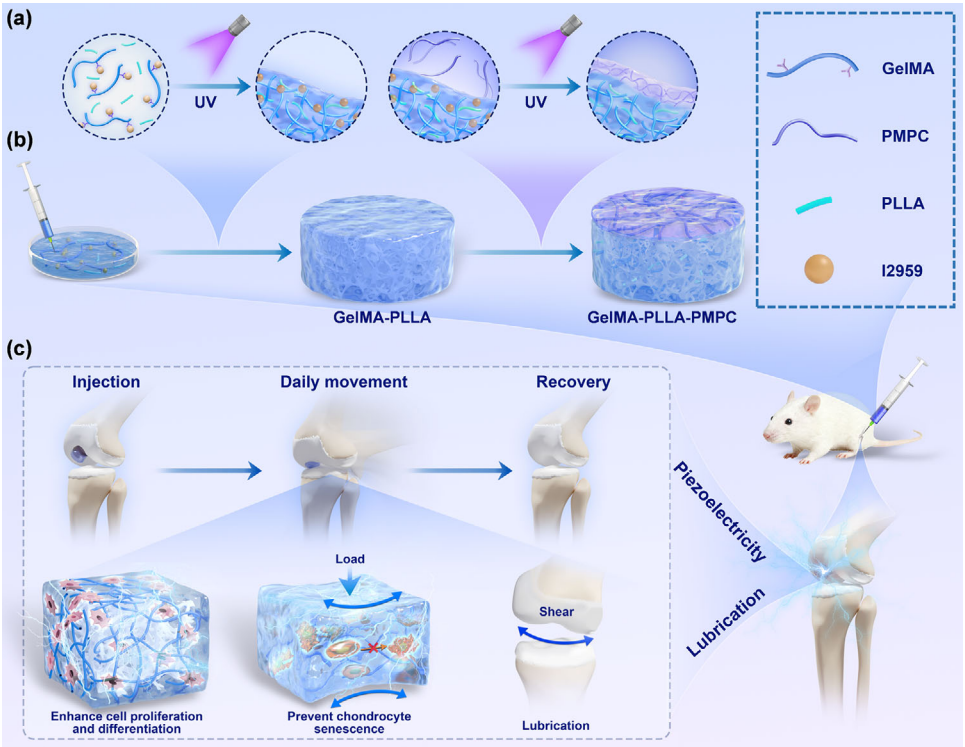

FIGURE 1 | Schematic diagram of the injectable and biodegradable lubricating piezoelectric hydrogel scaffold for synergistic osteochondral regeneration. (a) Synthesis mechanism of PMPC coating graft onto the GelMA surface through a shared photoinitiator strategy: the residual photoinitiator (I2959) on the cured GelMA surface serves as the active site to initiate the grafting of PMPC coating under UV irradiation. (b) Schematic of the fabrication process: under the same photocured condition, the GelMA-PLLA composite precursor is injected and photocured, followed by the in situ surface polymerization of the PMPC lubricating coating, forming the GelMA-PLLA-PMPC integrated scaffold. (c) Therapeutic mechanism in vivo: the injectable scaffold fills the cartilage defect. During daily joint movement, the surface PMPC layer provides lubrication to dissipate shear stress. Concurrently, the piezoelectric signals under compressive load synergistically prevent chondrocyte senescence and enhance cell proliferation and differentiation for osteochondral recovery.

remarkable reduction in COF is attributed to the unique molecular structure of PMPC, which contains a phosphatidylcholine group that forms a stable and ordered hydration layer with water molecules on the surface of the hydrogel. It effectively reduces the COF through the mechanism of hydration lubrication [28], which is crucial for mitigating wear and creating a protective environment essential for subsequent cartilage regeneration.

2.3 | Swelling and Degradation Properties

To evaluate the in vivo stability and biological relevance, the swelling and degradation behaviors of the three hydrogel formulations: GelMA (G), GelMA-PLLA (G-P), and GelMA-PLLA-PMPC (G-P-M) were comprehensively investigated. In an in vitro enzymatic degradation assay using a 1 mg/mL collagenase solution, the three hydrogel groups exhibited similar degradation profiles. After 21 days, each scaffold showed a weight loss rate approaching 75% (Figure 3a,b). At 37°C in phosphate-buffered saline (PBS), all three scaffolds retained approximately 30% of their mass after 49 days (Figure 3c; Figure S9).

Regarding swelling characteristics, all three hydrogels exhibited comparable behavior, reaching swelling equilibrium within 8 h (Figure 3d) while maintaining a stable form and good structural integrity throughout the process (Figure S10). Overall, all three hydrogels demonstrate prolonged in vivo retention, accommodating the entire course of cartilage repair prior to their biodegradation. This eliminates concerns regarding secondary surgical removal procedures.

2.4 | Rheological and Mechanical Properties

The mechanical properties of the hydrogels were systematically assessed via rheological and compression tests. Based on the rheological test results in Figure 3e,f, the storage modulus (G′) exceeds the loss modulus (G″), indicating that all three hydrogels exhibit predominantly elastic behavior and possess a certain degree of stability. Significantly, the incorporation of PLLA short fibers slightly increases the G′ value of the GelMA hydrogel, resulting in more advantageous mechanical properties. However, this also enhances the GelMA hydrogel's energy dissipation capacity, likely due to PLLA short fibers affecting the slip and recovery of the crosslinked network.

Furthermore, the prepared lubricating piezoelectric hydrogel exhibits excellent mechanical stability and deformation characteristics suitable for cartilage biomimicry (Figure 3g). Notably, the G-P-M hydrogel scaffold withstands 10 compression cycles without significant deformation or stress reduction (Figure 3h). This robust mechanical performance suggests the scaffold's

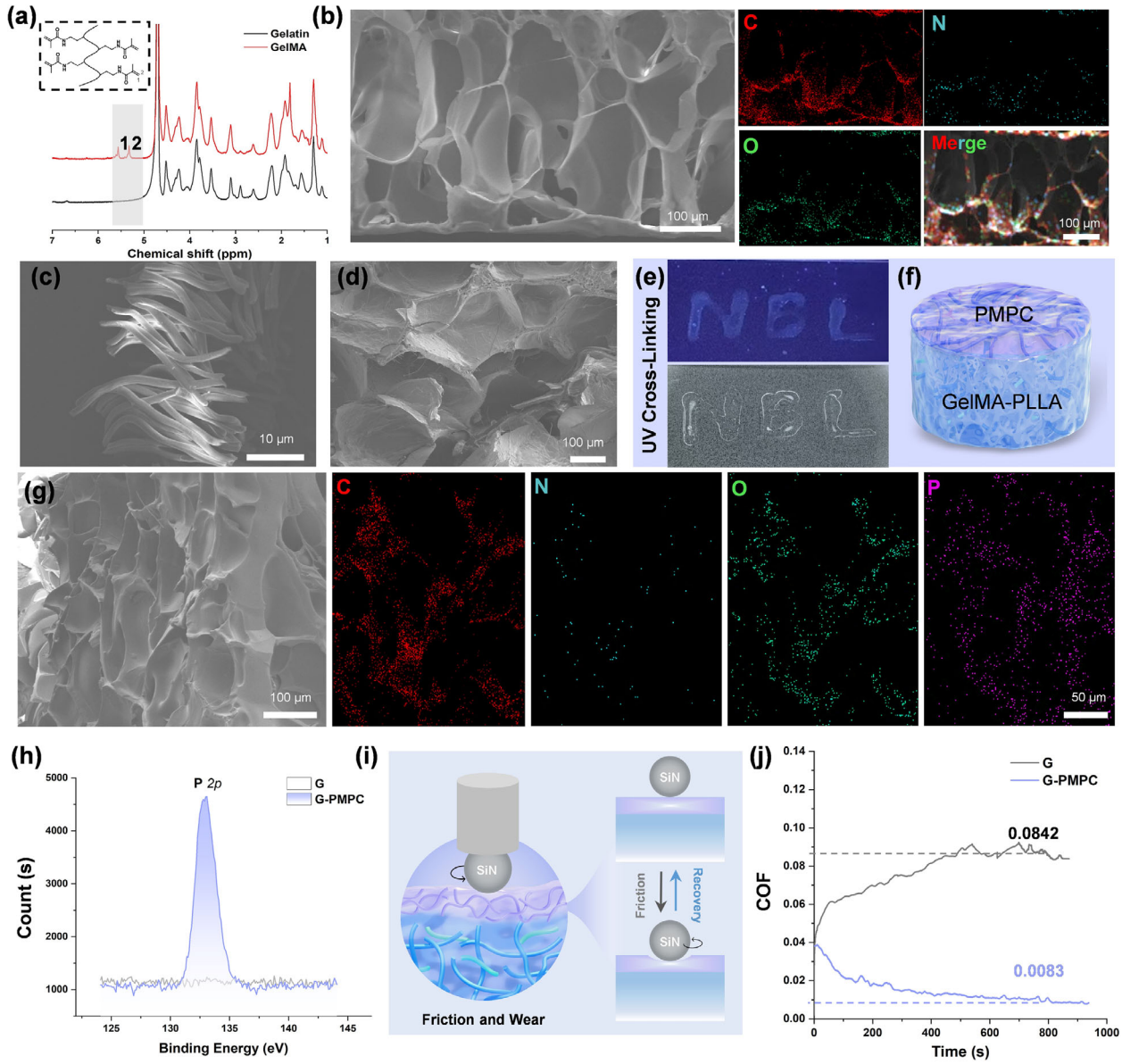

FIGURE 2 | Fabrication and characterization of the lubricating piezoelectric hydrogel. (a) ^{1}H NMR of the GelMA hydrogel prepared from gelatin. (b) The SEM image and element distribution of the GelMA hydrogel. SEM images of (c) PLLA short fibers and (d) GelMA-PLLA hydrogel. (e) Photographs of injectable GelMA-PLLA hydrogel during UV crosslinking and after crosslinking. (f) Schematic diagram of PMPC coating preparation on GelMA-PLLA hydrogel. (g) The SEM image and element distribution on the surface of the lubricating hydrogel. (h) Analysis of P Element in XPS Spectra of Hydrogels Before and After PMPC Modification. (i) Diagram of friction and wear on the lubricated hydrogel: When silicon nitride (SiN) spheres undergo rotational motion on the G-PMPC hydrogel, the phosphatidylcholine groups of the PMPC form a hydration layer that reduces friction. (j) COF curves of the GelMA hydrogel before and after PMPC modification.

ability to maintain its structural integrity and functional efficacy under dynamic loading conditions, crucial for enduring the physiological movements post-implantation.

2.5 | Electric Properties of Lubricating Hydrogels

The PLLA short fibers in the hydrogel serve as the piezoelectric component, with their piezoelectric properties originating from the electrospun PLLA fibers. We first characterized the intrinsic piezoelectric performance of the electrospun PLLA fibers, which served as the precursor for the short fibers. As shown in Figure S11, these PLLA nanofiber membranes could generate an open-circuit voltage of 1.45 V. Subsequently, different concentrations of short fibers (0, 1, 2, 5, and 10 mg/mL) were added to the GelMA hydrogel to sequentially prepare G-0, G-1, G-2, G-5, and G-10. To evaluate their piezoelectric response, these hydrogels were precisely fabricated into disc-shaped piezoelectric sensors with a diameter of 1 cm. The piezoelectric output was measured using vacuum-dried hydrogels to eliminate the short-circuiting effect caused by mobile ions in the hydrated state, which is a necessary and standard approach for accurately characterizing the intrinsic piezoelectricity of hydrogel networks [24]. Upon mechanical compression, the piezoelectric output

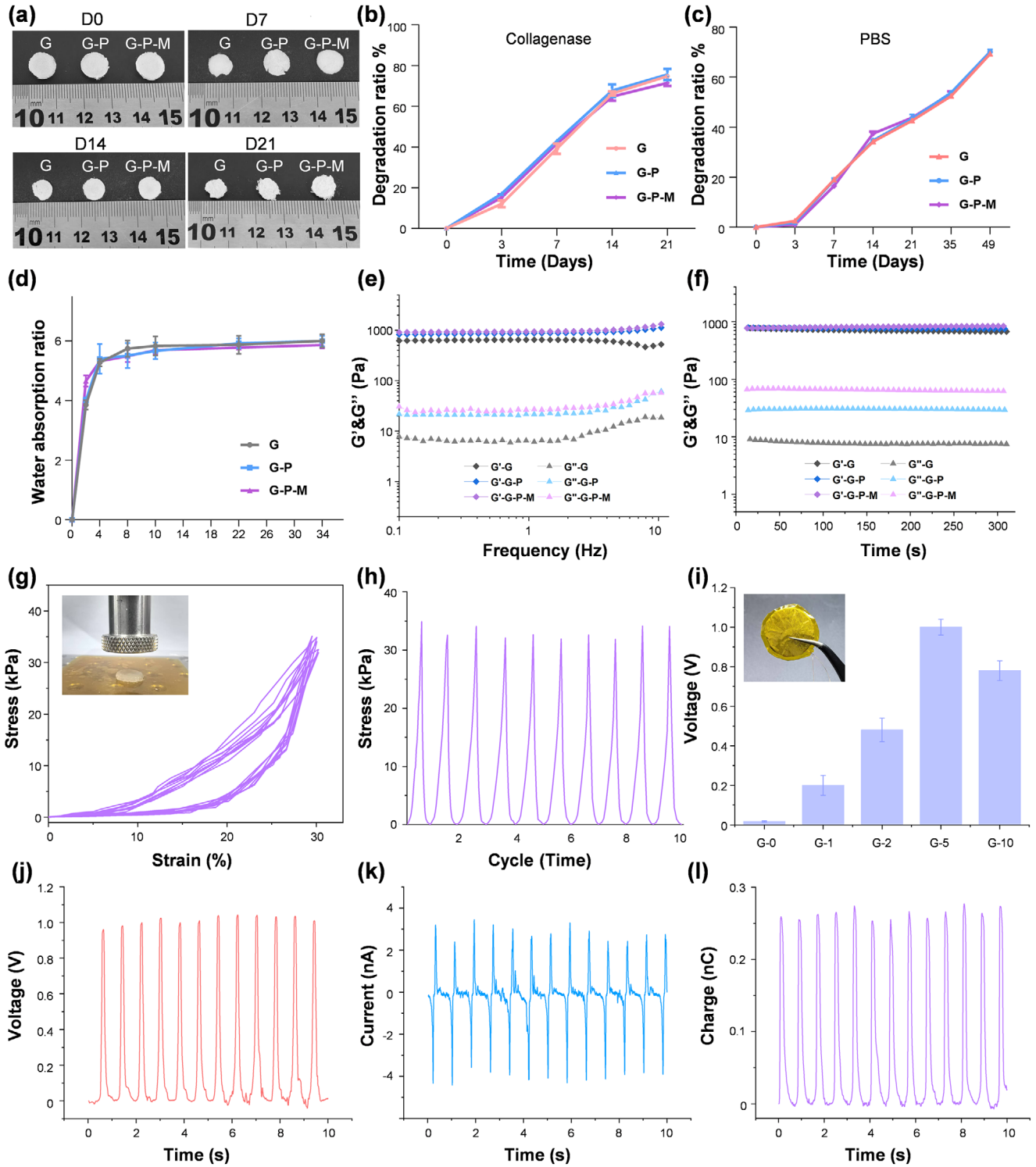

FIGURE 3 | Physical and chemical properties of the lubricating piezoelectric hydrogel. (a) Digital photographs and (b) Degradation curves of each hydrogel group degraded by collagenase at 1 mg/mL. (c) Degradation curves of each hydrogel group in 37°C PBS. (d) Swelling curves of each hydrogel group during 36 h. (e) Frequency sweep tests and (f) Time sweep tests of different hydrogels. (g) The cyclic compression stress–strain curves and (h) The stress in each cycle of the G-P-M hydrogel. (i) Piezoelectric output of GelMA hydrogels doped with different concentrations of PLLA short fibers. (j) The voltage output, (k) Current, and (l) Charge of the GelMA hydrogel doped with 5 mg/mL PLLA short fibers.

(voltage, current, and charge) from these devices was systematically measured. Figure 3i and Figure S12 indicate that the device output increases with the addition of PLLA short fibers, reaching a maximum value (approximately 1 V, 4.37 nA, and 0.25 nC) at 5 mg/mL (Figure 3j–l).

However, as the PLLA short fiber concentration further increased, the voltage at 10 mg/mL decreased to 0.7 V. This may be attributed to the high fiber density increasing the hydrogel mass, causing the charges generated by the fibers to cancel each other out and thereby reducing the piezoelectric output

[24]. Notably, the optimal PLLA concentration (5 mg/mL) was selected by maximizing the physical piezoelectric output. Because the inherently mild nature of localized piezoelectric cues is well below the typical thresholds of traditional external electrical stimulation [29, 30], our strategy prioritized maximizing the electrical output to ensure effective activation of cellular mechanotransduction pathways. After comprehensive consideration, a G-P hydrogel concentration of 5 mg/mL was ultimately selected for subsequent experiments. Furthermore, it was crucial to confirm that the subsequent grafting of the PMPC lubricating coating did not impair the established piezoelectric functionality. Indeed, the PMPC-modified G-P-M hydrogel demonstrated a comparable voltage output to the G-P hydrogel (Figure S13).

2.6 | Assessment of the Biocompatibility and Cell Proliferation

The biocompatibility of the hydrogels was evaluated using the material extract method. As shown in Figure S14, the CCK-8 assay revealed no statistically significant differences in the relative cell viability of chondrocytes among all groups. These results indicate that the constituent components of the scaffold exhibit excellent biocompatibility.

To investigate the synergistic bioactivity stemming from mechanical load and load-activated piezoelectricity, a custom dynamic cyclic compression device (Figure 4a) was employed to precisely mimic physiological loading conditions [31]. The experimental groups were designated as follows: Control, GelMA (G), GelMA-PLLA (G-P), GelMA with force (G+F), GelMA-PLLA with force (G−P+F).

Both chondrocytes and BMSCs were employed to assess the proliferation response of piezoelectric stimulation. For BMSCs, accelerated proliferation was observed in the G+F and G−P+F groups compared to the unloaded control groups (Figure 4b). Furthermore, the proliferation rate in the G−P+F group was significantly higher than that in the G+F group. The results clearly validate a synergistic effect between mechanical and electrical signals: the enhanced proliferation in the G+F group is attributed to cell activation via mechanotransduction pathways [32, 33], whereas the superior performance of the G−P+F group is due to the additional upregulation of cellular activity driven by the piezoelectric signals [34]. Similar trends were also observed for chondrocytes (Figure S15). Overall, these proliferation assays demonstrate the fundamental regulatory role of mechanical stimulation. More importantly, they reveal that under identical loading conditions, the synergistic integration of mechanical and electrical signals significantly amplifies the proliferative potential of cells, underscoring the distinct advantage of the piezoelectric scaffold.

2.7 | Evaluation of the Effect of Piezoelectric Stimulation on Cell Differentiation

The regeneration of bone and cartilage tissue is pivotal to successful osteochondral repair. The active recruitment of endogenous MSC is crucial for the effectiveness of the scaffold. Recent studies have reported that localized electrical cues generated by piezoelectric hydrogels under mechanical stimulation can actively recruit autologous stem cells [35, 36]. Therefore, we systematically evaluated the efficacy of mechanically activated piezoelectric stimulation in driving the osteogenic and chondrogenic differentiation of BMSCs.

For osteogenic differentiation, we initially assessed the expression of alkaline phosphatase (ALP), an early osteogenic marker [37]. ALP staining and activity assays (Figure 4c,d) revealed no significant differences among the G, G-P, and the control groups. Notably, ALP expression was significantly upregulated in the G+F group, while the G−P+F group exhibited the highest expression levels. This trend was further verified by the deposition of mineralized nodules, a late-stage marker of osteogenesis (Figure 4c,e), where the degree of mineralization in the G−P+F group was markedly superior to that of all other groups, demonstrating the synergistic effect of mechanical and piezoelectric cues.

For chondrogenic differentiation, Alcian Blue staining was employed to assess the deposition of glycosaminoglycan (GAG), a key component of cartilage extracellular matrix (Figure 4c). Results indicated that GAG accumulation was most robust in the G−P+F group, demonstrating its superior capacity for chondrogenic induction compared to all other conditions.

To elucidate the underlying pro-differentiation mechanisms, we further investigated the pro-differentiation mechanism at the molecular level. Immunofluorescence staining revealed that the relative fluorescence intensities of the chondrogenic transcription factor SOX9 and the osteogenic transcription factor RUNX2 were significantly higher in the G−P+F group compared to the G+F group (Figure 4f,g). This trend was confirmed by qPCR analysis, which showed maximal expression levels of chondrogenic genes (ACAN, Col2A1) and osteogenic genes (OPN, RUNX2) in the G−P+F group (Figure 4h). The osteogenic and chondrogenic differentiation of BMSCs is driven by a multifaceted mechanotransduction mechanism. First, piezoelectric stimulation can induce the autocrine secretion of endogenous transforming growth factors (e.g., TGF-β) to initiate differentiation [38]. Second, these piezoelectricity triggers the opening of specific membrane ion channels, notably voltage-gated calcium channels (VGCCs) and Piezo1, facilitating a rapid intracellular calcium influx. This calcium transient serves as a crucial second messenger that activates downstream signaling cascades, ultimately directing the differentiation of BMSCs [39, 40].

Collectively, these findings demonstrate that while moderate mechanical loading provides a basal stimulus for maintaining cell homeostasis, the combined and synergistic action of mechanical and load-activated piezoelectric stimulation profoundly promotes the lineage-specific differentiation of BMSCs toward both osteogenic and chondrogenic phenotypes.

2.8 | Piezoelectric Stimulation Inhibits Chondrocyte Senescence In Vitro

Chondrocyte senescence is a critical pathological process, contributing not only to cartilage repair failure but also serving

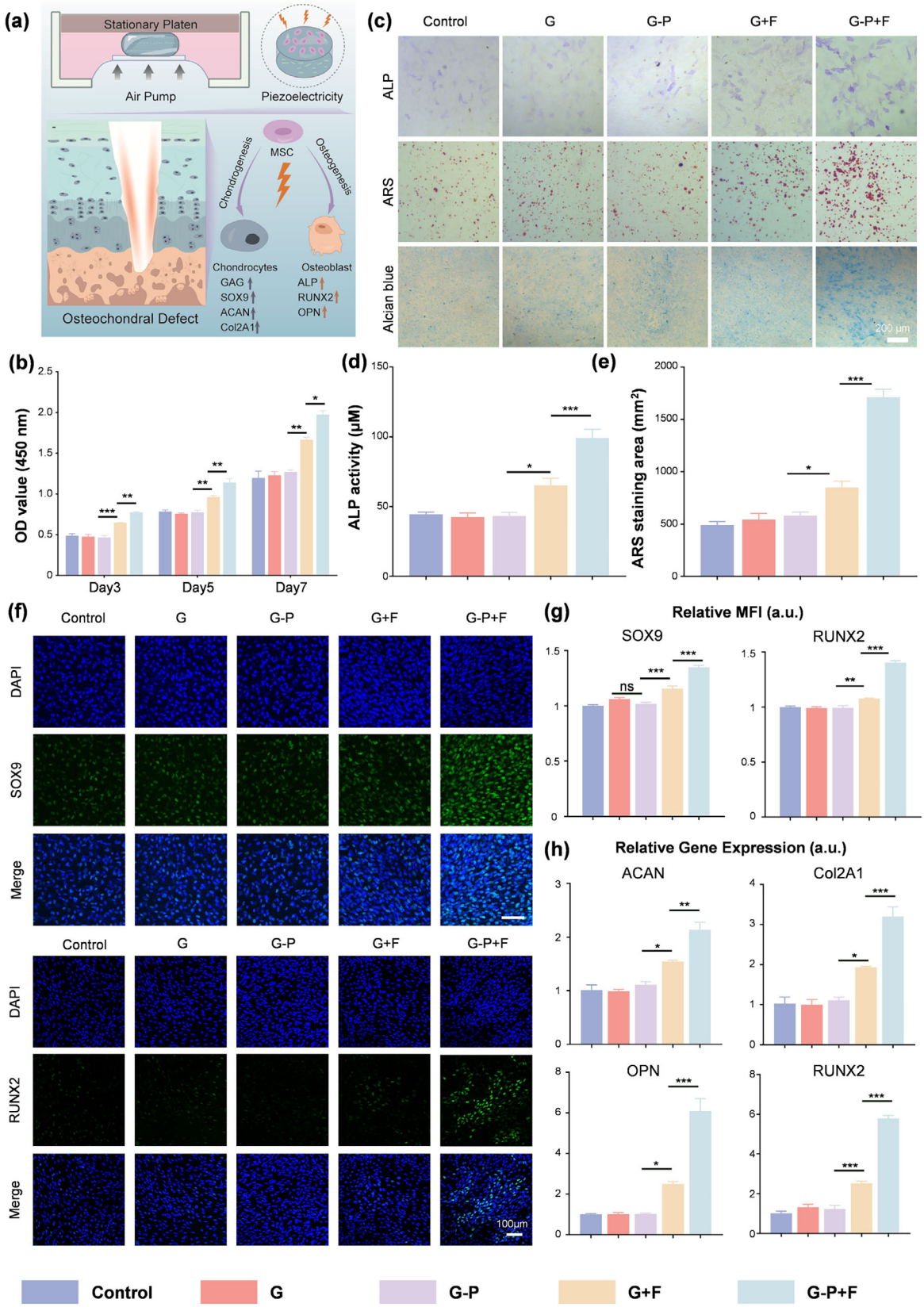

FIGURE 4 | In vitro evaluation of cytocompatibility and differentiation. (a) Schematic diagram of the mechanism of the simulation of load-activated piezoelectricity. (b) Cell viability of MSC assessed by CCK-8 assay at days 3, 5, and 7. (c) Representative images of ALP staining (day 7), ARS staining (day 14), and Alcian Blue staining (day 7) across different groups. (d) Quantitative analysis of ALP activity. (e) Quantitative analysis of calcium nodule area based on ARS staining. (f) Representative immunofluorescence images of SOX9 and RUNX2. (green: SOX-9 or RUNX2; blue: DAPI). (g) Quantitative analysis of relative mean fluorescence intensity (MFI) h) Relative gene expression of chondrogenic (ACAN, Col2A1) and osteogenic (OPN, RUNX2) markers. Data are presented as mean ± SEM. $^{*}p < 0.05$, $^{**}p < 0.01$, $^{***}p < 0.001$.

as a pivotal trigger of osteoarthritis (OA) [41]. Mechanical loading plays a paradoxical role in cartilage homeostasis. While appropriate physiological loading is a crucial physical signal for maintaining cartilage homeostasis, excessive mechanical stimulation—particularly when local stress concentration occurs due to damaged articular interfaces—is a significant inducer of cell senescence [42]. Although improving interface lubrication can effectively dissipate excessive shear stress to mitigate physical damage [43], we hypothesize that harnessing physiological loading to activate endogenous piezoelectric signals offers a more proactive and profound therapeutic potential for actively inhibiting senescence (Figure 5a).

To this end, we established a chondrocyte senescence model in vitro and applied cyclic compression to verify the senescence-alleviating efficacy of piezoelectric stimulation [44]. SA-β-Gal activity is widely recognized as a specific biomarker for identifying senescent cells. The staining results indicated that the G+F group moderately inhibited chondrocyte senescence to some extent, while the G−P+F group exhibited the most significant anti-senescent effect, minimizing the number of senescent cells (Figure 5b,c). To further investigate the molecular mechanisms, we examined key characteristics of chondrocyte senescence: irreversible cell cycle arrest and the expression of senescence-associated secretory phenotype (SASP) factors, which collectively lead to ECM catabolism and disrupt tissue homeostasis [16]. We performed immunofluorescence characterization of cell cycle arrest markers (p16, p21) and a critical SASP factor (MMP13) (Figure 5b,d). Mean fluorescence intensity (MFI) analysis revealed that while the G+F group exhibited a moderate inhibitory effect on the senescence phenotype, the expression levels of those markers were significantly further downregulated in the G−P+F group.

Collectively, these findings strongly suggest that while mechanical lubrication helps mitigate physical damage, the active electromechanical stimulation provided by our piezoelectric hydrogel effectively attenuates the progression of microenvironmental deterioration and actively inhibits the pathological senescence of chondrocytes. This active inhibition of senescence is likely mediated by the suppression of the NF-κB signaling pathway. The activation of the NF-κB pathway is recognized as a primary driver of chondrocyte senescence [45]. Importantly, electrical stimulation has been demonstrated to inhibit NF-κB nuclear translocation [46]. This biophysical suppression effectively downregulates the downstream cellular senescence cascade. Furthermore, the activation of the TGF-β/Smad 2/3 signaling pathway may also contribute to the overall anti-senescent and chondroprotective effects [34].

2.9 | In Vivo Synergistic Enhancement of Osteochondral Regeneration

Based on the previous findings, we used the G-P-M hydrogel scaffold to evaluate the in vivo synergistic efficacy of lubrication and piezoelectricity. The G-P-M scaffold integrates passive mechanical shielding with active piezoelectric stimulation. As a biomimetic boundary, the superficial PMPC layer utilizes superlubricity to dictate selective stress transfer. By attenuating pathological shear stress, it prevents localized mechanical overload. On the one hand, the lubrication layer establishes a low-stress microenvironment to preserve the nascent cartilage matrix. On the other hand, it maintains the structural integrity of the bulk GelMA hydrogel, preventing premature scaffold degradation and ensuring the long-term stability of the embedded PLLA fibers in situ. Consequently, the intact network continuously transduces physiological compressive loads into piezoelectric signals, providing sustained electrical stimuli for tissue regeneration. To validate the efficacy, a rat full-thickness osteochondral defect model was established, and animals were divided into five experimental groups: Defect, GelMA (G), GelMA-PMPC (G-M), GelMA-PLLA (G-P), and GelMA-PLLA-PMPC (G-P-M). Corresponding scaffolds were implanted, and repair outcomes were assessed at 4 and 8 weeks post-surgery (Figure 6a).

Macroscopic observation at both time points (Figure 6b) revealed negligible repair in the untreated Defect group, with the lesion remaining clearly concave. The G group exhibited partial tissue filling; the regenerated surface appeared rough and irregular. The G-M and G-P groups showed enhanced filling and smoother surfaces compared to the G group, but no significant differences were observed between these two groups regarding macroscopic cartilage surface repair. In contrast, the G-P-M group achieved optimal repair, regenerating a smooth articular surface that integrated seamlessly with the surrounding host tissue, yielding the highest International Cartilage Repair Society (ICRS) scores (Figure 6b,e).

Micro-computed tomography (Micro-CT) analysis further corroborated these findings, demonstrating that the G-P-M group exhibited superior subchondral bone regeneration and the highest bone volume fraction (BV/TV) (Figure 6b,d). Notably, although the G-M and G-P groups displayed comparable outcomes in cartilage surface repair, the G-P group had better repair than the G-M group in terms of subchondral bone formation. This result indicated the specific capacity of piezoelectric stimulation to actively promote the regeneration of deep subchondral bone [47].

2.10 | Histological Evaluation of Tissue Regeneration

Histological analysis was performed to thoroughly evaluate tissue regeneration within the osteochondral defects. Initial hematoxylin and eosin (H&E) staining (Figure 6c) revealed no significant inflammatory response across any of the experimental groups. The Defect group was predominantly occupied by fibrous tissue, whereas the G group, despite showing marginal improvement over the Defect group, still exhibited significant concave depressions. While the G-M and G-P groups showed tissue filling, cellular arrangement remained disorganized, and the integration interface with the host tissue was distinct, indicating incomplete integration. In contrast, the G-P-M group achieved complete regeneration and full integration of the defect area by week 8.

Further analysis with Toluidine Blue and SO/FG staining (Figure 6f), which highlights proteoglycan content, indicated that the G-P-M group exhibited the most robust GAG accumulation. Modified O'Driscoll scoring confirmed that the G-P-M group

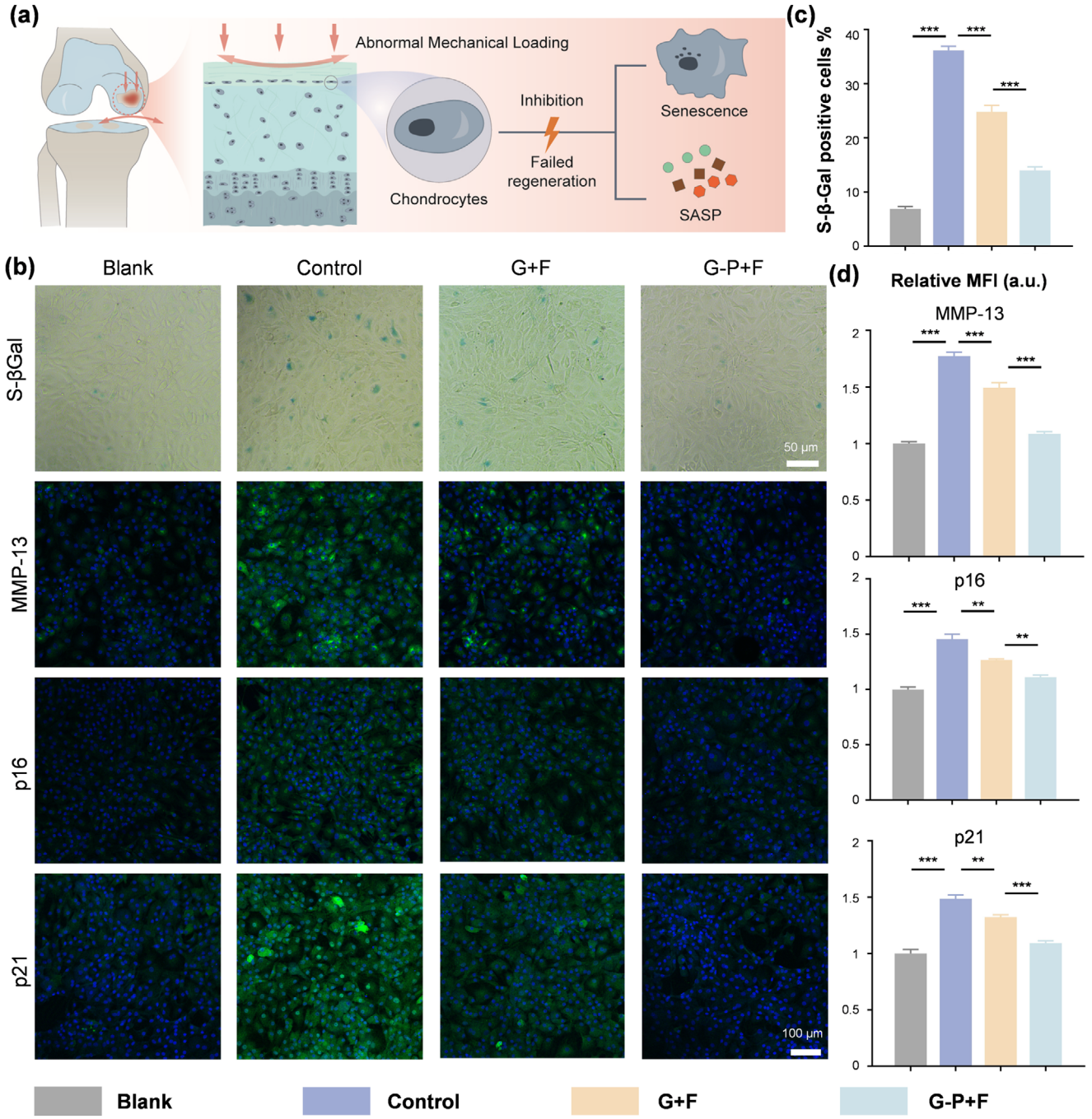

FIGURE 5 | Piezoelectric stimulation inhibits chondrocyte senescence in vitro. (a) Schematic diagram of the mechanism of piezoelectric stimulation in chondrocyte senescence. (b) Images of SA-β-Gal staining and immunofluorescence staining for MMP13, p16, and p21. (green: MMP-13, p16 or p21; blue: DAPI). (c) Quantification of the percentage of SA-β-Gal positive cells. (d) Quantitative analysis of the relative MFI for MMP13, p16, and p21. Data are presented as mean ± SEM. $^{*}p < 0.05$, $^{**}p < 0.01$, $^{***}p < 0.001$.

yielded the highest scores (Figure 6g). Notably, the G-P group scored significantly higher than the G-M group. These results suggest that although piezoelectric stimulation can promote osteochondral regeneration, a poorly lubricated cartilage surface is susceptible to shear-induced damage. The PMPC coating effectively dissipated harmful frictional forces to create a low-stress microenvironment, thereby protecting the nascent cartilage matrix induced by piezoelectric signals [48]. Although breaching the subchondral bone recruits endogenous BMSCs via a microfracture-like mechanism, in situ photocuring retains these cells within the hydrogel [49]. However, microfracture alone typically yields fibrocartilage; functional restoration demands active lineage guidance. By providing synergistic surface lubrication and load-activated piezoelectric stimulation, the scaffold guides these endogenous BMSCs toward distinct osteochondral lineages, ultimately translating spontaneous cell recruitment into functional joint restoration.

Further examination using Sirius Red staining under polarized light revealed that the collagen fiber arrangement of the G-P-M

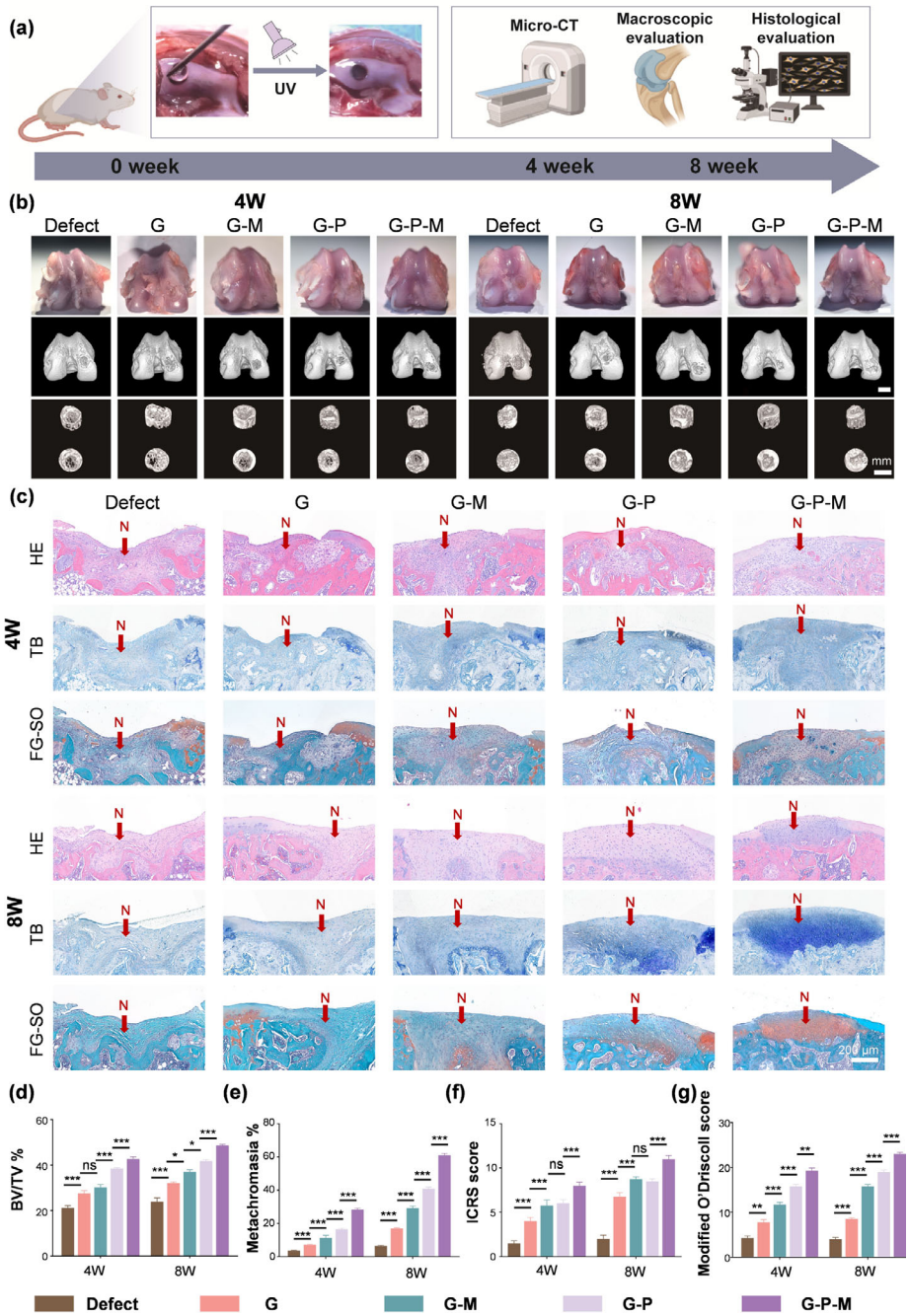

FIGURE 6 | In vivo evaluation of osteochondral regeneration in a rat model. (a) Diagram of the experimental design. (b) Macroscopic observations of the femoral condyle and representative Micro-CT 3D reconstructions and 2D cross-sectional images at 4 and 8 weeks post-surgery. (c) Representative H&E, Toluidine Blue (TB), and Safranin O-Fast Green (SO/FG) staining images of regenerated tissues at 4 and 8 weeks (N: newly generated tissue). (d) Quantitative analysis of the BV/TV. (e) ICRS score of the regenerated tissue. (f) Quantitative analysis of metachromasia of the FG-SO. (g) Histological evaluation using the Modified O'Driscoll score. Data are presented as mean ± SEM. $^{*}p < 0.05$, $^{**}p < 0.01$, $^{***}p < 0.001$.

group exhibited a structure similar to native cartilage (Figure 7a). The superficial layer displayed horizontal alignment, facilitating load buffering and lubrication, while the deep layer showed vertical alignment, enhancing the transition to subchondral bone and providing load-bearing support [50]. To determine the spatial specificity of the regenerated tissue, we characterized the expression of type II alpha 1 (Col2A1) and osteocalcin (OCN) (Figure 7b). Both markers were significantly upregulated in the G-P-M group, but the distribution showed distinct spatial patterns. Col2A1 was extensively distributed throughout the upper regenerated cartilage matrix, indicating the formation of hyaline-like cartilage, while the osteogenic marker OCN was primarily enriched in the lower subchondral bone region. This indicates that the native in vivo microenvironment acts as the primary driver for spatial lineage commitment. Rather than simply forcing a single lineage, piezoelectric stimulation functions as a biophysical amplifier that magnifies these distinct endogenous cues, thereby activating spatially appropriate osteochondral regeneration [51]. Statistical analysis (Figure 7d) confirmed that the percentage of OCN-positive area in the G-P-M group was significantly

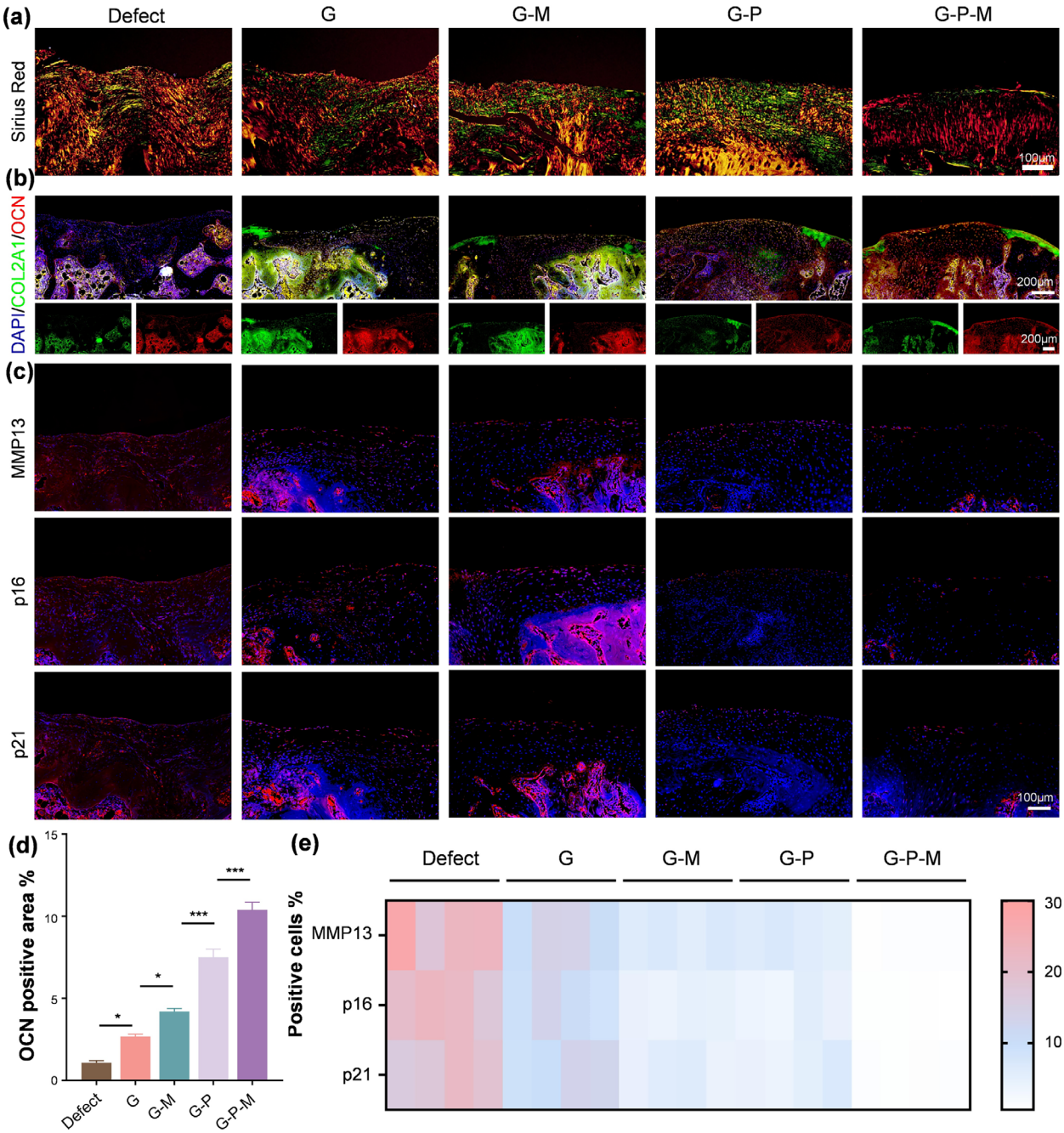

FIGURE 7 | Histological and immunofluorescence analysis of tissue integration. (a) Representative Sirius Red staining, (b) Immunofluorescence staining for cartilage-bone interface markers (green: Col2A1; red: OCN; blue: DAPI), (c) Senescence-associated markers (green: MMP13, p16, p21; blue: DAPI) in the defect regions at 8 weeks. (d) Statistical analysis of OCN-positive area percentage in cartilage-bone interface. (e) Heatmap quantifying the percentage of cells positive for MMP-13, p16, and p21. Data are presented as mean ± SEM. $^{*}p < 0.05$, $^{**}p < 0.01$, $^{***}p < 0.001$.

higher than in other groups. This indicates that the scaffold effectively induced subchondral bone remodeling concurrently with cartilage regeneration, achieving stable integration at the osteochondral interface.

Finally, given the inhibitory role of the senescent microenvironment in osteochondral regeneration, we examined the expression of senescence-associated markers: MMP13, p16, and p21. Immunofluorescence results (Figure 7c) revealed elevated expression of these markers in the Defect and G groups, indicating severe chondrocyte senescence. Conversely, quantitative heatmap analysis (Figure 7e) demonstrated a marked reduction in the proportion of positive cells in the G-P-M group. These results suggest that the G-P-M scaffold effectively modulates the local microenvironment, inhibiting cellular senescence and catabolism to provide favorable physiological conditions for long-term, stable cartilage regeneration. The scaffold prevents mechanically-induced senescence through a synergy of passive lubrication and active piezoelectricity. While pathological overload drives chondrocyte senescence, the superficial PMPC layer effectively dissipates these destructive forces [52]. The preserved physiological loads are subsequently transduced by the PLLA

into electrical signals, preventing the senescent cascade and promoting cartilage repair.

3 | Conclusions

In conclusion, we have successfully developed a novel biodegradable and injectable hydrogel scaffold (G-P-M) that precisely integrates synergistic piezoelectric stimulation and surface lubrication for osteochondral defect repair. Leveraging a streamlined two-step in situ photocuring process, this scaffold offers convenient, minimally invasive implantation.

The innovative design of the G-P-M scaffold addresses a critical challenge in joint tissue engineering by achieving a distinct mechanical synergy. Its superficial PMPC lubricating coating functions as an intelligent mechanical filter, effectively dissipating detrimental shear stress to safeguard cells from friction-induced damage. Simultaneously, this targeted stress dissipation ensures the selective transmission of beneficial physiological compressive loads to the internal PLLA piezoelectric network, thereby generating localized, in situ electrical signals crucial for tissue regeneration.

Comprehensive in vitro assessments demonstrated the scaffold's excellent biocompatibility and highlighted its multifaceted bioactivity. Specifically, mechanically activated piezoelectric stimulation significantly enhanced the osteogenic and chondrogenic differentiation of BMSCs. Furthermore, the G-P-M scaffold uniquely prevents chondrocyte senescence through a dual anti-senescence mechanism: a passive inhibition via shear reduction (lubrication) and an active inhibition via piezoelectric regulation of cellular pathways (cell cycle and phenotype modulation).

Crucially, in vivo evaluations using a rat full-thickness osteochondral defect model corroborated these in vitro findings, validating that the synergistic effect of lubrication and piezoelectric stimulation not only promoted robust osteochondral regeneration but also profoundly attenuated cartilage senescence. This multifunctional scaffold thus achieves superior and sustained repair efficacy by simultaneously optimizing the mechanical and electrophysiological microenvironments. Our study, therefore, offers a bioinspired strategy for developing advanced regenerative therapies, presenting a promising avenue for clinical cartilage regeneration and joint preservation.

4 | Experimental Section

4.1 | Preparation and Characterization of GelMA Hydrogel

GelMA hydrogel precursor solution was prepared by reacting gelatin (Sigma, USA) and methacrylic anhydride (Aladdin, China). The synthesis procedure follows: Briefly, 5 g of gelatin was dissolved in 50 mL of phosphate-buffered saline (PBS) (Solarbio, China) to prepare a 10% (w/v) gel precursor solution. After thorough dissolution in a 50°C water bath, slowly add 8 mL of methacrylic anhydride and continue stirring for 1 h under light-protected conditions. The reaction was terminated with excess PBS, followed by sequential dialysis and freeze-drying. The synthesis of GelMA hydrogel was verified by hydrogen nuclear magnetic resonance (NMR) spectroscopy. The product was dissolved in PBS to prepare a 10% GelMA solution. Subsequently, 0.1 wt.% I2959 (Aladdin, China) was added as an initiator. Under UV irradiation at 365 nm, the solution underwent curing and cross-linking to form a GelMA hydrogel. The morphologies and element distribution of the prepared GelMA hydrogel were characterized by scanning electron microscopy (SEM) (SU8020, Hitachi) and elemental mapping, respectively.

4.2 | Preparation and Characterization of PLLA Short Fibers

First, PLLA (Esunmed, China) was dissolved in Hexafluoroisopropanol (HFP) (Aladdin, China) to prepare a 10% (w/v) spinning precursor solution. Electrospinning was performed at an applied voltage of 15 kV and a flow rate of 1 mL/h, maintaining a 15 cm gap between the needle tip and the collector. A rotating drum collector operating at 2,000 rpm is used to obtain the aligned PLLA nanofiber membrane. Subsequently, the PLLA membrane was annealed in a 150°C oven for 12 h, yielding the final piezoelectric PLLA membrane. The annealed PLLA membrane was embedded using a cryoembedding agent (4583, SAKURA, Japan) and cut into short fibers (30 μm) using a freezing microtome (CM3050S, Leica). After washing with deionized water, these products underwent freeze-drying to obtain PLLA short fibers. The morphology and size of the PLLA short fibers were observed using SEM.

To verify that PLLA short fibers can be effectively mixed with the prepared GelMA (G-P) hydrogel, the morphologies of the G-P hydrogel were characterized by SEM, and the injectability was verified.

4.3 | Preparation and Characterization of the Lubricating Piezoelectric Hydrogel

The residual photoinitiator of 2-hydroxy-4′-(2-hydroxyethoxy)-2-methylpropiophenone (I2959) (Macklin, China) within the GelMA hydrogel can induce the surface radical polymerization of 2-(methacryloyloxy)ethyl 2-(trimethylammonio)ethyl phosphate (MPC) (Macklin, China). Briefly, a 10 wt.% MPC solution (dissolved in PBS) was poured onto the surface of the G-P hydrogel. Subsequently, the hydrogel was further UV-irradiated under 365 nm UV light for 10 min to obtain the lubricating piezoelectric hydrogel (G-P-M). The surface morphology and elemental distribution of the G-P-M hydrogel were evaluated by SEM and EDS mapping, respectively. The successful polymerization of PMPC on the hydrogel surface was confirmed by X-ray photoelectron spectroscopy (XPS; ESCALAB 250Xi, Thermo Fisher Scientific) and Fourier-transform infrared spectroscopy (FTIR; Nicolet 8700, Thermo Fisher Scientific)

The presence of PMPC also confers lubricating properties to the G-P-M hydrogel. A friction and wear tester (UMT TriboLab, Bruker) is used to assess the lubricating effect of PMPC coating on hydrogels.

4.4 | Swelling and Degradation Assays

To evaluate the swelling ratio, hydrogels were prepared into 1 cm diameter lyophilized discs (weighed as W_0) and immersed in sterile PBS at 37°C. After 48 h, the samples were removed, gently wiped to remove surface water (weighed as W_t). The swelling ratio was calculated as $(W_t - W_0)/W_0 \times 100\%$. To evaluate in vitro degradation, samples with a diameter of 1 cm were submerged in PBS and maintained at 37°C in an incubator for 3 weeks. Accelerated enzymatic degradation was also evaluated by incubating samples in PBS containing 1 mg/mL type II collagenase (Sigma, USA). The mass changes of each hydrogel group throughout the entire degradation process were recorded.

4.5 | Rheological Behaviors and Mechanical Properties

An MCR 302 rheometer (Anton-Paar, Austria) was used to determine the rheological behaviors at 25°C, with the gap set to 1 mm. Frequency scan testing was conducted at a 1% strain condition within the frequency range of 0.1–100 Hz. Time scan tests were performed at a constant frequency of 1 Hz and 1% strain for 300 s. The storage modulus (G′) and loss modulus (G″) were recorded.

The compressive properties of hydrogels were evaluated using an ESM301/Mark-10 tensile testing system. The hydrogel with a diameter of 1 cm were subjected to cyclic compression tests at a rate of 5 mm min^{-1}, with 10 repeated compression experiments conducted within the 0%–30% strain range to evaluate the hydrogel's mechanical strength and fatigue resistance.

4.6 | Piezoelectric Properties of the Lubricating Piezoelectric Hydrogel

First, the piezoelectric properties of the annealed PLLA fiber membrane were evaluated. The PLLA fiber membrane was cut into 1.5 × 1.5 cm rectangles and coated with conductive aluminum tape on both sides to serve as electrodes. Copper wires were connected to the electrodes on opposite sides, and the entire assembly was sealed with polyimide (PI, DuPont) tape to form a piezoelectric sensor. The output electrical signal was measured directly using an electrometer (Keithley 6517) and an oscilloscope (HDO 6104). Similarly, the piezoelectric properties of hydrogels containing PLLA short fibers at different concentrations were also tested. After drying, each group of samples (Ø = 1 cm) was prepared and encapsulated, and then the piezoelectric tests were conducted following the same protocol as described above.

4.7 | Cell Isolation and Culture

Primary rat chondrocytes were isolated as previously described [53]. Briefly, knee cartilage was harvested from neonatal Sprague-Dawley (SD) rats. The cartilage tissue was digested with 0.25% trypsin (Solarbio, China) with 37°C, 5% CO_2 incubation for 30 min to remove excessive soft tissue. Subsequently, the cartilage tissue was cut into small pieces and incubated overnight in a medium containing 0.2 mg/mL collagenase. After centrifugation, the isolated chondrocytes were cultured in chondrocyte growth medium, which was low-glucose DMEM (Solarbio, China) containing 10% fetal bovine serum (FBS) (Moni, China), and 1% penicillin-streptomycin (Solarbio, China). Chondrocytes between passages 1 (P1) and 3 (P3) were used for subsequent experiments.

Mesenchymal stem cells (MSCs) were isolated from the calvaria of neonatal SD rats [54]. The tissue was minced and digested with 0.1 mg/mL type II collagenase for 30 min at 37°C. The cell suspension was centrifuged and co-cultured with bone fragments until 90% confluency with MSC culture medium, which was α-MEM (Solarbio, China) containing 10% FBS, and 1% penicillin-streptomycin. For MSC differentiation, Chondrogenic differentiation medium was prepared by supplementing MSC culture medium with 1 mM sodium pyruvate (Sigma, USA), 10 ng/mL TGF-β3 (MedChemExpress, USA), 0.1 μM dexamethasone (Solarbio, China), 1% ITS cell culture supplement (Oricellbio, China), 1 μM 2-Phospho-L-ascorbic acid (Solarbio, China). The osteogenic induction medium was formulated by adding 0.5 mM ascorbic acid, 10 μM dexamethasone, and 10 mM β-glycerophosphate to the basal MSC medium.

To apply mechanical stimulation, cell-laden gels were placed between the silicone elastomer bottoms of BioFlex culture plates (Flexcell, USA) and a stationary platen. An air pump was used to cyclically deflect the membrane at a frequency of 1 Hz for 20 min per day.

4.8 | Cell Viability and Proliferation Assessment

Cell viability and proliferation were determined using a Cell Counting Kit-8 (CCK-8) assay. At the Days 3 and 7, the culture medium was replaced with 10% CCK-8 solution (Solarbio, China). Absorbance at 450 nm was recorded using a microplate reader (Varioskan, Thermo Fisher) after the samples were incubated in the dark at 37°C for 15 min. Data were normalized to the control group to determine cell viability and proliferation.

4.9 | Alkaline Phosphatase (ALP) Activity Assessment

After 7 days of osteogenic induction, the ALP activity of the MSCs was evaluated. ALP activity was assessed using ALP Assay Kit (Beyotime, China) according to the manufacturer's instruction. The absorbance was measured at the wavelength of 405 nm ($n = 3$).

4.10 | ALP, Alizarin Red S (ARS), Alcian Blue Staining

ALP and Alizarin Red S (ARS) staining were used to evaluate osteogenic differentiation, while Alcian Blue staining was used to assess chondrogenic differentiation. ALP and Alcian Blue staining were performed on day 7, and ARS staining was performed on day 14. Briefly, after fixation with 4% paraformaldehyde (PFA) (Beyotime, China) for 20 min, cells were respectively stained with the ALP Stain Kit (Solarbio, China), ARS solution (Solarbio, China), and Alcian Blue Staining Kit (Beyotime, China)

according to the manufacturer's instructions. The quantitative analysis of the ARS staining area was performed using ImageJ software ($n = 3$).

4.11 | Cell Immunofluorescence Staining

In brief, the cells were subjected to fixation using 4% PFA for 20 min, followed by permeabilization with 0.3% Triton X-100 for 5 min. Subsequently, blocking was performed using 5% BSA in PBS for 1 h at room temperature. Cells were then incubated overnight at 4°C with primary antibodies against: SOX9 (1:500, Abcam, USA; chondrogenic marker), RUNX2 (1:400, Cell Signaling Technology, USA; osteogenic marker), p16INK4a (1:100, Invitrogen, USA; senescence marker), p21 (1:50, Invitrogen, USA; senescence marker), and MMP13 (1:200, Invitrogen, USA; SASP component). Subsequently, cells were incubated with Alexa Fluor 488-conjugated goat anti-rabbit IgG (1:1000, Abcam, USA) for 1 h at room temperature in the dark. Nuclei were counterstained with DAPI (1:200, Solarbio, China) for 5 min. Images were captured using a confocal microscope (Leica SP8), and the mean fluorescence intensity (MFI) was quantified using ImageJ software ($n = 4$).

4.12 | Real-Time Quantitative PCR

Total RNA was extracted from cultured cells using TRIzol reagent (Beyotime, China) according to the manufacturer's instructions. The concentration and purity of the RNA were quantified using a NanoDrop (Thermo Fisher). cDNA was synthesized from total RNA using the HiScript II Q RT SuperMix (Vazyme, China). The resulting cDNA was then amplified using Taq Pro Universal SYBR qPCR Master Mix (Vazyme, China) and specific primers (Synthesized by Tsingke Biotechnology; sequences listed in Table S1). Quantitative real-time PCR (qPCR) was subsequently performed using a real-time PCR detection system (QuantGene 9600, Bioer Technology). The relative mRNA expression levels were normalized by the expression of β-actin and calculated using $2^{-\Delta\Delta Ct}$ method ($n = 3$).

4.13 | Chondrocyte Senescence Induction

To induce senescence, P3 chondrocytes were treated with 10 ng/mL IL-1β (MedChemExpress, USA) and 50 μM H_2O_2 (Aladdin, China) for 48 h [37]. Senescence-associated β-Galactosidase (SA-β-Gal) staining was performed using an SA-β-Gal Staining Kit (Beyotime, China) according to the manufacturer's instructions. Images were captured using a light microscope. The percentage of SA-β-Gal positive cells was quantified using ImageJ ($n = 4$).

4.14 | Animal Experiment

Eight-week-old male Sprague-Dawley (SD) rats were purchased from SPF Biotechnology Co., Ltd. (Beijing, China). All animal procedures were approved by the Committee on Ethics of Small Animal Experimental Platform of National Key Laboratory (No. 2024005LZ). A full-thickness cylindrical osteochondral defect (1.5 mm in diameter and 1.5 mm in depth) was created in the femoral medial condyle of the knee joint. All animals were randomly divided into five groups: defect, G, G-M, G-P, G-P-M ($n = 4$). For the treatment groups, the hydrogels were implanted. All animals were allowed free activity. Animals were euthanized at 4 and 8 weeks post-surgery, and the knee joints were harvested for subsequent analysis. ICRS macroscopic cartilage repair score was used to assess the macroscopic cartilage repair (Table S2).

4.15 | Micro-Computed Tomography (Micro-CT) Evaluation

To evaluate subchondral bone regeneration, the harvested femoral tissues were scanned using micro-CT system (PE Quantum GX, Perkin Elmer) at 25 μm voxel size, 90 kV voltage, and 88 μA current. The tissues were reconstructed, and the bone volume (BV)/ tissue volume (TV) was quantified using Analyze 11.0 (Perkin Elmer, USA).

4.16 | Histological Analysis

The femoral condyle tissues were fixed in 4% PFA, followed by decalcification, dehydration, and embedded in paraffin and sectioned into slices. Histological evaluation of cartilage regeneration was performed using H&E, Safranin O/Fast Green (SO/FG), Toluidine Blue (TB), and Sirius Red (SR) stains. Modified O'Driscoll Score was applied for the evaluation of histological regeneration (Table S3). For immunofluorescence staining, sections were incubated with primary antibodies including p16INK4a, p21, and MMP13 and secondary antibody. Immunofluorescence images were captured using a confocal microscope.

4.17 | Statistical Analysis

All data are presented as the means ± standard error of the means (SEM.). Statistical analysis was performed using GraphPad Prism 9.0 (GraphPad Software, USA). Differences among multiple groups were assessed using One-way analysis of variance (ANOVA) followed by Tukey's post-hoc test. A p-value <0.05 was considered statistically significant (* for $p < 0.05$, ** for $p < 0.01$, *** for $p < 0.001$).

Author Contributions

Yantao Zhao and Zhou Li supervised the project, provided resources, and reviewed the manuscript. All authors have read and agreed to the published version of the manuscript. Yusheng Li and Yadong Zhang conceived and designed the experiments. Dengjie Yu and Longfei Li performed the experiments, analyzed the data, and wrote the original draft. Xi Cui contributed to the original draft writing and the manuscript revision. Binbin Yang, Boyang Pei, and Jiaxuan Li provided technical support for material design and characterization. Ruizeng Luo assisted with the animal surgery.

Acknowledgements

This work was supported by the Research and Translational Application of Clinical Characteristic Diagnosis and Treatment Techniques in the

Capital (Z221100007422014), the National Natural Science Foundation of China (T2125003, 82272493, U25A20417), Beijing Natural Science Foundation (L245015, Z240022, L256001, 25JL006), and Hunan Provincial Science Fund for Distinguished Young Scholars (No. 2024JJ2089).

Conflicts of Interest

The authors declare no conflicts of interest.

Data Availability Statement

The data that support the findings of this study are available from the corresponding author upon reasonable request.

References

1. E. A. Makris, A. H. Gomoll, K. N. Malizos, J. C. Hu, and K. A. Athanasiou, "Repair and Tissue Engineering Techniques for Articular Cartilage," *Nature Reviews Rheumatology* 11 (2015): 21–34, https://doi.org/10.1038/nrrheum.2014.157.

2. A. M. Bhosale and J. B. Richardson, "Articular Cartilage: Structure, Injuries and Review of Management," *British Medical Bulletin* 87 (2008): 77–95, https://doi.org/10.1093/bmb/ldn025.

3. N. K. Arden, T. A. Perry, R. R. Bannuru, et al., "Non-Surgical Management of Knee Osteoarthritis: Comparison of ESCEO and OARSI 2019 Guidelines," *Nature Reviews Rheumatology* 17 (2021): 59–66, https://doi.org/10.1038/s41584-020-00523-9.

4. S. Muthu, J. V. Korpershoek, E. J. Novais, G. F. Tawy, A. P. Hollander, and I. Martin, "Failure of Cartilage Regeneration: Emerging Hypotheses and Related Therapeutic Strategies," *Nature Reviews Rheumatology* 19 (2023): 403–416, https://doi.org/10.1038/s41584-023-00979-5.

5. A. R. Armiento, M. Alini, and M. J. Stoddart, "Articular Fibrocartilage—Why Does Hyaline Cartilage Fail to Repair," *Advanced Drug Delivery Reviews* 146 (2019): 289–305, https://doi.org/10.1016/j.addr.2018.12.015.

6. H. Kwon, W. E. Brown, C. A. Lee, et al., "Surgical and Tissue Engineering Strategies for Articular Cartilage and Meniscus Repair," *Nature Reviews Rheumatology* 15 (2019): 550–570, https://doi.org/10.1038/s41584-019-0255-1.

7. D. Yu, Q. Nie, J. Xue, et al., "Direct Mapping of Cytomechanical Homeostasis Destruction in Osteoarthritis Based on Silicon Nanopillar Array," *Advanced Healthcare Materials* 12 (2023): 2301126, https://doi.org/10.1002/adhm.202301126.

8. Q. Du, S. Su, H. Dai, et al., "Physical Biomedical Science: A New Field of Original Interdisciplinary Research," *Chinese Science Bulletin* 69 (2024): 2008–2014.

9. X. Deng, Y. Zhuang, J. Cui, et al., "Open Challenges and Opportunities in Piezoelectricity for Tissue Regeneration," *Advanced Science* 12, no. 38 (2025): 10349, https://doi.org/10.1002/advs.202510349.

10. X. Cui, L. Wu, C. Zhang, and Z. Li, "Implantable Self-Powered Systems for Electrical Stimulation Medical Devices," *Advanced Science* 12 (2025): 2412044, https://doi.org/10.1002/advs.202412044.

11. X. Cui, Y. Shan, J. Li, et al., "Bifunctional Piezo-Enhanced PLLA/ZA Coating Prevents Aseptic Loosening of Bone Implants," *Advanced Functional Materials* 34 (2024): 2403759, https://doi.org/10.1002/adfm.202403759.

12. Y. Liu, G. Dzidotor, T. T. Le, et al., "Exercise-Induced Piezoelectric Stimulation for Cartilage Regeneration in Rabbits," *Science Translational Medicine* 14, no. 627 (2022): abi7282, https://doi.org/10.1126/scitranslmed.abi7282.

13. D. Liu, X. Wang, C. Gao, et al., "Biodegradable Piezoelectric-Conductive Integrated Hydrogel Scaffold for Repair of Osteochondral Defects," *Advanced Materials* 36 (2024): 2409400.

14. K. Watanabe, H. Mutsuzaki, T. Fukaya, et al., "Simulating Knee-Stress Distribution Using a Computed Tomography-Based Finite Element Model: A Case Study," *Journal of Functional Morphology and Kinesiology* 8, no. 1 (2023): 15, https://doi.org/10.3390/jfmk8010015.

15. W. Lin and J. Klein, "Recent Progress in Cartilage Lubrication," *Advanced Materials* 33 (2021): 2005513, https://doi.org/10.1002/adma.202005513.

16. P. R. Coryell, B. O. Diekman, and R. F. Loeser, "Mechanisms and Therapeutic Implications of Cellular Senescence in Osteoarthritis," *Nature Reviews Rheumatology* 17 (2021): 47–57, https://doi.org/10.1038/s41584-020-00533-7.

17. J. D. Humphrey, E. R. Dufresne, and M. A. Schwartz, "Mechanotransduction and Extracellular Matrix Homeostasis," *Nature Reviews Molecular Cell Biology* 15 (2014): 802–812, https://doi.org/10.1038/nrm3896.

18. S. Yao, X. Cui, C. Zhang, W. Cui, and Z. Li, "Force-Electric Biomaterials and Devices for Regenerative Medicine," *Biomaterials* 320 (2025): 123288, https://doi.org/10.1016/j.biomaterials.2025.123288.

19. R. Xie, H. Yao, A. S. Mao, et al., "Biomimetic Cartilage-Lubricating Polymers Regenerate Cartilage in Rats With Early Osteoarthritis," *Nature Biomedical Engineering* 5 (2021): 1189–1201, https://doi.org/10.1038/s41551-021-00785-y.

20. R. Luo, Y. Xiong, J. Li, et al., "Piezoelectric Injectable Anti-Adhesive Hydrogel to Promote Endogenous Healing of Tendon Injuries," *Advanced Materials* 37 (2025): 2501306, https://doi.org/10.1002/adma.202501306.

21. K. Dey, S. Agnelli, and L. Sartore, "Designing Viscoelastic Gelatin-Peg Macroporous Hybrid Hydrogel With Anisotropic Morphology and Mechanical Properties for Tissue Engineering Application," *Micro* 3 (2023): 434–457.

22. V. K. Panneer Selvam, T. Fukunaga, Y. Suzuki, et al., "Single-Cell Screening Through Cell Encapsulation in Photopolymerized Gelatin Methacryloyl," *Micro* 4 (2024): 295–304.

23. C. Gao, W. Dai, X. Wang, et al., "Magnesium Gradient-Based Hierarchical Scaffold for Dual-Lineage Regeneration of Osteochondral Defect," *Advanced Functional Materials* 33 (2023): 2304829, https://doi.org/10.1002/adfm.202304829.

24. T. Vinikoor, G. K. Dzidotor, T. T. Le, et al., "Injectable and Biodegradable Piezoelectric Hydrogel for Osteoarthritis Treatment," *Nature Communications* 14 (2023): 6257, https://doi.org/10.1038/s41467-023-41594-y.

25. R. Luo, Y. Xiong, J. Li, et al., "Piezoelectric Injectable Anti-Adhesive Hydrogel to Promote Endogenous Healing of Tendon Injuries," *Advanced Materials* 37 (2025): 2501306, https://doi.org/10.1002/adma.202501306.

26. W. Lin, M. Kluzek, N. Iuster, et al., "Cartilage-Inspired, Lipid-Based Boundary-Lubricated Hydrogels," *Science* 370 (2020): 335–338, https://doi.org/10.1126/science.aay8276.

27. Y. Wang, Y. Xu, W. Zhai, et al., "In-Situ Growth of Robust Superlubricated Nano-Skin on Electrospun Nanofibers for Post-Operative Adhesion Prevention," *Nature Communications* 13 (2022): 5056, https://doi.org/10.1038/s41467-022-32804-0.

28. Y. Xue, X. Niu, J. Zhou, L. Wang, and Y. Fan, "Recent Development in Understanding the Role of Lipids in Cartilage Lubrication," *Friction* 13 (2025): 9441014, https://doi.org/10.26599/FRICT.2025.9441014.

29. J. Sun, W. Xie, Y. Wu, Z. Li, and Y. Li, "Accelerated Bone Healing Via Electrical Stimulation," *Advanced Science* 12, no. 24 (2025): 2404190, https://doi.org/10.1002/advs.202404190.

30. K. Varani, F. Vincenzi, S. Pasquini, et al., "Pulsed Electromagnetic Field Stimulation in Osteogenesis and Chondrogenesis: Signaling Pathways and Therapeutic Implications," *International Journal of Molecular Sciences* 22, no. 2 (2021): 809, https://doi.org/10.3390/ijms22020809.

31. D. Liu, X. Wang, C. Gao, et al., "Biodegradable Piezoelectric-Conductive Integrated Hydrogel Scaffold for Repair of Osteochondral Defects," *Advanced Materials* 36 (2024): 2409400, https://doi.org/10.1002/adma.202409400.

32. Y.-W. Chen, Y.-H. Lin, T.-L. Lin, K.-X. A. Lee, M.-H. Yu, and M.-Y. Shie, "3D-Biofabricated Chondrocyte-Laden Decellularized Extracellular

Matrix-Contained Gelatin Methacrylate Auxetic Scaffolds Under Cyclic Tensile Stimulation for Cartilage Regeneration," *Biofabrication* 15, no. 4 (2023): 045007, https://doi.org/10.1088/1758-5090/ace5e1.

33. Y. Ge, Y. Li, Z. Wang, L. Li, H. Teng, and Q. Jiang, "Effects of Mechanical Compression on Chondrogenesis of Human Synovium-Derived Mesenchymal Stem Cells in Agarose Hydrogel," *Frontiers In Bioengineering and Biotechnology* 9 (2021): 697281, https://doi.org/10.3389/fbioe.2021.697281.

34. Z. Lin, L. Nan, H. Lu, et al., "Print-And-Roll Hierarchically Structured Piezoelectric Scaffolds for Exercise-Driven Cartilage Regeneration," *Advanced Functional Materials* 35 (2025): 2424448, https://doi.org/10.1002/adfm.202424448.

35. Y.-B. Liu, X. Liu, X.-F. Li, et al., "Multifunctional Piezoelectric Hydrogels Under Ultrasound Stimulation Boost Chondrogenesis by Recruiting Autologous Stem Cells and Activating the Ca^{2+}/Cam/Can Signaling Pathway," *Bioactive Materials* 50 (2025): 344–363, https://doi.org/10.1016/j.bioactmat.2025.04.009.

36. Z. Han, F. Wang, W. Xiong, et al., "Precise Cell Type Electrical Stimulation Therapy Via Force-Electric Hydrogel Microspheres for Cartilage Healing," *Advanced Materials* 37 (2025): 2414555.

37. J. Tian, R. Shi, Z. Liu, et al., "Self-Powered Implantable Electrical Stimulator for Osteoblasts′ Proliferation and Differentiation," *Nano Energy* 59 (2019): 705–714, https://doi.org/10.1016/j.nanoen.2019.02.073.

38. Y. Liu, G. Dzidotor, T. T. Le, et al., "Exercise-Induced Piezoelectric Stimulation for Cartilage Regeneration in Rabbits," *Science Translational Medicine* 14 (2022): abi7282.

39. Y. W. Li, J. Chen, S. B. Liu, et al., "Biodegradable Piezoelectric Polymer for Cartilage Remodeling," *Matter* 7 (2024): 1631–1643.

40. D. Liu, X. Wang, C. Gao, et al., "Biodegradable Piezoelectric-Conductive Integrated Hydrogel Scaffold for Repair of Osteochondral Defects," *Advanced Materials* 36, no. 45 (2024): 2409400, https://doi.org/10.1002/adma.202409400.

41. B. O. Diekman and R. F. Loeser, "Aging and the Emerging Role of Cellular Senescence in Osteoarthritis," *Osteoarthritis And Cartilage* 32 (2024): 365–371, https://doi.org/10.1016/j.joca.2023.11.018.

42. Y. Shao, H. Zhang, H. Guan, et al., "Pdzk1 Protects Against Mechanical Overload-Induced Chondrocyte Senescence and Osteoarthritis by Targeting Mitochondrial Function," *Bone Research* 12, no. 1 (2024): 41, https://doi.org/10.1038/s41413-024-00344-6.

43. X. Chen, H. Cao, H. Lei, et al., "Janus Graphene Oxide Nanoplatform With Oppositely Functionalized Adhesion and Lubrication Enables Local Sustained Fenofibrate Release to Synergistically Halt Osteoarthritis," *Advanced Materials* 38, no. 4 (2026): 14327, https://doi.org/10.1002/adma.202514327.

44. C. Deng, L. Yu, X. Zhao, et al., "Genetically Engineered Chondrocyte-Mimetic Nanoplatform Attenuates Osteoarthritis by Blocking Il-1β and Restoring Sirtuin-3," *Science Advances* 11 (2025): adv4238, https://doi.org/10.1126/sciadv.adv4238.

45. L. Jie, Y. Zhang, J. Liu, et al., "PINK1 Overexpression Suppresses P38 MAPK/NF-Kb Signaling to Attenuate Chondrocyte Senescence in Osteoarthritis," *International Journal of Molecular Medicine* 56, no. 6 (2025): 1–15, https://doi.org/10.3892/ijmm.2025.5665.

46. M. Lee, H. Lee, H. Chung, et al., "Micro-Current Stimulation Could Inhibit Il-1β-Induced Inflammatory Responses in Chondrocytes and Protect Knee Bone Cartilage From Osteoarthritis," *Biomedical Engineering Letters* 14 (2024): 801–812, https://doi.org/10.1007/s13534-024-00376-1.

47. X. Cui, L. Xu, Y. Shan, et al., "Piezocatalytically-Induced Controllable Mineralization Scaffold With Bone-Like Microenvironment to Achieve Endogenous Bone Regeneration," *Science Bulletin* 69 (2024): 1895–1908, https://doi.org/10.1016/j.scib.2024.04.002.

48. R. L. Trevino, C. A. Pacione, A.-M. Malfait, S. Chubinskaya, and M. A. Wimmer, "Development of a Cartilage Shear-Damage Model to Investigate the Impact of Surface Injury on Chondrocytes and Extracellular Matrix Wear," *Cartilage* 8 (2017): 444–455, https://doi.org/10.1177/1947603516681133.

49. K. Mithoefer, T. McAdams, R. J. Williams, P. C. Kreuz, and B. R. Mandelbaum, "Clinical Efficacy of the Microfracture Technique for Articular Cartilage Repair in the Knee," *The American Journal of Sports Medicine* 37 (2009): 2053–2063, https://doi.org/10.1177/0363546508328414.

50. A. Pueyo Moliner, K. Ito, F. Zaucke, D. J. Kelly, M. de Ruijter, and J. Malda, "Restoring Articular Cartilage: Insights From Structure, Composition and Development," *Nature Reviews Rheumatology* 21 (2025): 291–308, https://doi.org/10.1038/s41584-025-01236-7.

51. J. Na, Z. Yang, Q. Shi, et al., "Extracellular Matrix Stiffness as an Energy Metabolism Regulator Drives Osteogenic Differentiation in Mesenchymal Stem Cells," *Bioactive Materials* 35 (2024): 549–563.

52. W. Xiong, Z. Han, S. L. Ding, et al., "In Situ Remodeling of Efferocytosis Via Lesion-Localized Microspheres to Reverse Cartilage Senescence," *Advanced Science* 11 (2024): 2400345.

53. M. Gosset, F. Berenbaum, S. Thirion, and C. Jacques, "Primary Culture and Phenotyping of Murine Chondrocytes," *Nature Protocols* 3 (2008): 1253–1260, https://doi.org/10.1038/nprot.2008.95.

54. H. Zhu, Z.-K. Guo, X.-X. Jiang, et al., "A Protocol for Isolation and Culture of Mesenchymal Stem Cells From Mouse Compact Bone," *Nature Protocols* 5 (2010): 550–560, https://doi.org/10.1038/nprot.2009.238.

Supporting Information

Additional supporting information can be found online in the Supporting Information section.

Supporting File: adfm75561-sup-0001-SuppMat.docx.